Thermomechanically coupled theory in the context of the multiphase-field method

Andreas Prahs [a,*], Martin Reder [a,b], Daniel Schneider [b,c], Britta Nestler [a,b,c]

[a] *Institute for Applied Materials - Microstructure Modelling and Simulation (IAM-MMS), Karlsruhe Institute of Technology (KIT), Straße am Forum 7, Karlsruhe, 76131, Baden-Württemberg, Germany*
[b] *Institute of Digital Materials Science (IDM), Karlsruhe University of Applied Sciences, Moltkestraße 30, Karlsruhe, 76133, Baden-Württemberg, Germany*
[c] *Institute of Nanotechnology - Microstructure Simulations (INT-MS), Karlsruhe Institute of Technology (KIT), Hermann-von-Helmholtz-Platz 1, Eggenstein-Leopoldshafen, 76344, Baden-Württemberg, Germany*

ARTICLE INFO

Keywords:
Thermoplasticity
Thermomechanical coupling
Growth of inclusion
Multiphase-field method
Greenwood–Johnson effect

ABSTRACT

The modeling and simulation of microstructure evolution is usually subject to the multiphase-field method. In this context, thermomechanical coupling is often neglected, even when non-isothermal phase transformations are considered. Using a simplified example, the present work shows that this assumption is not justified for small strains and small strain rates with respect to a non-vanishing coefficient of thermal expansion. To this end, both a thermomechanically coupled and a thermomechanically weakly coupled theory are briefly revisited. The difference between the coupled and the weakly coupled theory regarding the growth of an inclusion is discussed. The considered elastoplastic inclusion, subjected to eigenstrains, is embedded in an elastoplastic matrix under load. It is shown, that the weakly coupled theory overestimates the growth of the inclusion, and, thus, the volume concentration, compared to the coupled theory. Moreover, only the application of the coupled theory reflects a load-induced anisotropic growth of the inclusion, which exhibits an isotropic material behavior, due to non-vanishing uniaxial Neumann boundary conditions. In addition, it is shown that the smaller the heat conduction coefficient, the more pronounced the anisotropic growth of the inclusion.

1. Introduction

Motivation In computational materials science and microstructure mechanics, the characterization of materials by numerical methods is often based on scans of the microstructure such as EBSD or μ-CT scans. An alternative is given by digital microstructures, exhibiting the same characteristics as the scanned ones, obtained by microstructure modeling and subsequent simulation. Clearly, both modeling and simulation must provide a quantitative representation of the scanned microstructures in order for them to be used as digital surrogates. To this end, it is of utmost importance to understand in detail the mechanisms controlling the evolution of the microstructure.

Thermomechanically coupled and weakly coupled theory In the case of a thermomechanically coupled theory (TCT), both the balance of linear momentum and the heat conduction equation are mutually dependent. In this context, the balance of linear momentum is coupled to the equation of heat conduction by means of a thermoelastic formulation of Hooke's law. Moreover, for an elastoplastic material behavior, the equation of heat conduction accounts for, e.g., the plastic stress power density and thermomechanical coupling terms as heat sources or heat sinks, respectively, cf., e.g., [1, p.67]. Consequently, the solution of a boundary value problem (BVP) in the context of the TCT requires the solution of both, the balance of linear momentum and the equation of heat conduction, either in a monolithic or in a staggered manner. The heat source due to plastic deformation becomes more significant the higher the deformation rate [2]. Thus, TCT-approaches are commonly applied in the context of large deformations, regarding, e.g., shape memory alloys under cyclic loading [3,4], multi-phase transformations [5], the characterization of Portevin–Le Châtelier bands [6], recrystallization [7,8], or crystal plasticity [9]. In contrast, for an elastoplastic material, a thermomechanically weakly coupled theory (TWT) only allows for a coupling in the sense that the equation of heat conduction accounts for the plastic stress power. However, thermomechanical coupling terms are not taken into account. Moreover, Hooke's law does not account for thermal strains. Consequently, a thermomechanical BVP can be solved by two separate simulations: First the balance of linear momentum is solved and, subsequently, the obtained solution can be used as input for the heat conduction problem.

* Corresponding author.
E-mail address: andreas.prahs@kit.edu (A. Prahs).
URL: https://www.iam.kit.edu/mms/Mitarbeiter_5283.php (A. Prahs).

A. Prahs et al. Clearly, the TWT represents a truncation of the TCT. Regarding small strains and small (plastic) strain rates, the heating due to a deformation is negligibly small, cf. [2, Fig. 5]. This justifies the application of a TWT in the small strain regime, as commonly done in simulations of microstructure mechanics, cf., e.g., [10,11] in the context of a gradient crystal plasticity. However, the thermomechanical coupling should not be neglected unless the coefficient of thermal expansion is negligibly small, if an additional phase transformation is considered, as illustrated in the present work.

Multiphase-field method The multiphase-field method (MPFM), as an extension of the classical phase-field method (PFM) to several phases, cf., e.g., [12–14], is a numerically highly efficient method that is widely used for the simulation of microstructure evolution. The field of application includes, among other, phase transitions such as liquid–liquid, liquid–solid, and solid–solid, cf., e.g., [15–17]. With respect to the latter, e.g., solidification, cf., e.g., [18,19], growth of precipitations, cf., e.g., [20,21], recrystallization, cf., e.g., [22–24], and crack propagation, cf., e.g., [17,25–27] are considered. While coupling the classical (M)PFM with the heat conduction is possible, cf., e.g., [28, p.47], [29, Eq.(3.19)], and [30, p.179], a vast amount of publications focus on isothermal phase transitions and processes. Works that account for non-isothermal phase transitions discuss, e.g., thermal effects on the morphology evolution during crystallization, cf., e.g., [31], shape memory effects, cf., e.g., [32], and the simulation of hot-cracking, cf., e.g., [27]. However, none of these works account for a TCT: The evolution of the phase-field is coupled with the heat conduction equation by Wang et al. [31, Eqs. (6) & (16)]; The heat source is related to the accumulated plastic strain, however, neither thermomechanical coupling terms nor a thermoelastic Hooke's law is considered by Cissé and Asle Zaeem [32, Eqs. (10), (30) & (31)]; While a thermoelastic Hooke's law is considered, no thermomechanical coupling terms enter the equation of heat conduction in [27, Eqs. (11), (12) & (42)]. Even a non-isothermal phase-field model used for the simulation of thermally and stress induced martensitic transformations does neither account for thermal strains and, thereby, a thermoelastic Hooke's law, nor for thermomechanical coupling terms cf. [33, Eqs. (7), (8) & (13)]. Consequently, the effect of the thermomechanical coupling in the context of a TCT on the microstructure evolution, especially on the growth kinetics and the evolution of the shape of an inclusion, regarding a phase transformation is rarely discussed in literature. In the present work, the multiphase-field model according to Steinbach et al. [12] and Steinbach and Pezzolla [13], and Nestler et al. [14] is applied. The key findings of this work can be transferred to other phase-field models as well.

Greenwood-Johnson effect A prominent example for a phase transformation due to plastification is the so called Greenwood–Johnson (GJ) effect, cf., e.g., [34], representing one of two significant mechanisms [35] with respect to the behavior of steels that exhibit transformation induced plasticity (TRIP) behavior [36,37]. In this context, a load is applied to a composite consisting of a martensitic inclusion subjected to a distortion within an austenitic matrix. The load is significantly smaller than the yield stress of the austenitic matrix. Under the applied load, the martensitic inclusion grows at the expense of the austenitic matrix, which undergoes plastic deformation before the transformation takes place. The plastification of the matrix material can be accounted for using classical Mises plasticity [38], but also by use of more sophisticated plasticity models such as crystal plasticity theory [39–42], cf., e.g., [43–45]. In contrast to classical plasticity, the plastic deformation caused by the growth of the martensitic inclusion is referred to as transformation plasticity, cf., e.g., [46] regarding a micromechanical discussion of the GJ effect. The displacive transformation of this stress driven transformation is extensively studied in literature, cf., e.g., [47–49], and [50] in the context of the phase-field method, as well as Mahnken et al. [5,51], and Cheng and Mahnken [52] regarding the sharp interface context. The martensitic transformation, representing a displacive, i.e., diffusionless process, takes places at sonic speed. Consequently, diffusive processes are negligible.

Effect on the predicted effective material properties Regarding the overall mechanical behavior, TRIP steels are considered as composites with an austenitic matrix and martensitic inclusions [53]. In this context, it is known that the volume content of the martensite is of utmost importance with respect to the effective (plastic) mechanical properties [54,55]. In addition, the shape of the martensitic inclusions within an underlying microstructure also significantly affects the effective material properties [56]. Microstructure simulations, used to generate digital surrogates for further investigations, necessarily have to predict the volume fraction of martensite as well as the shape of martensitic inclusions as precisely as possible.

Objective of the current work The main objective of the present work is to elaborate how the simulated microstructure is affected by TCT compared to TWT, with respect to the growth kinetics and the shape of the inclusion. To this end, the concept of a TCT and a TWT are revisited, at first. Both the TWT and the TCT are applied in the context of MPFM. The effect of using a TCT in contrast to a TWT with respect to the transformation-induced growth of an elastoplastic inclusion, subjected to a distortion, within an elastoplastic matrix under load is discussed. As an instructive trivial form, a setup mimicking the GJ effect is considered for the simulations, where the distortion of the inclusion is accounted for by transversely isotropic eigenstrains, for simplicity. Moreover, the variation of the parameters leading to these differences and associated implications are considered. Possible consequences for the effective (predicted) material properties are briefly addressed. To restrict the attention to the effect of the thermomechanical coupling, the plastification of the matrix material is accounted for by a classical Mises plasticity without hardening. It should be emphasized that the objective of the present work is not the in-depth, quantitative modeling or simulation of martensitic phase transformation. Therefore, the constitutive material behavior and the considered setup are kept as simple as possible, by intention: Only two phases are considered; Different orientations between the phases are not taken into account. For a more elaborated setup, the impact of using TCT instead of TWT is expected to be greater than for the simple setup discussed here.

Originality Part of the originality of the present work is the application of TCT to the growth of an elastoplastic inclusion, subject to eigenstrains, in an elastoplastic matrix under load. As a major novelty of the present work, it is shown that the application of TWT cannot be justified by considering small strains or small (plastic) strain rates when phase transformations are considered and the coefficient of thermal expansion is not negligible. Regarding the growth kinetics of the inclusion, it is shown that the application of the TWT leads to an overestimation of the growth behavior, i.e., the inclusion grows faster. Furthermore, it is shown that only the application of TCT reflects an anisotropic growth of the inclusion due to anisotropic boundary conditions which are realized by non-vanishing uniaxial Neumann boundary conditions. It is emphasized that the material behavior of both inclusion and matrix is considered to be isotropic. Thus, the load-induced, anisotropic growth of the inclusion is directly related to the applied boundary condition and is only accounted for by the application of the TCT. The application of the TWT leads to an isotropic growth of the inclusion.

Outline In Section 2, the concepts of a TCT and a TWT are briefly revisited . In this context, the thermodynamical prerequisites of the TCT and the TWT are discussed, as well as the fundamentals on the considered MPFM and the corresponding treatment/implementation of plasticity. For a comparison between the results obtained by TCT and TWT, a setup that mimics the GJ effect, the corresponding simulations, a variation of parameters leading to these differences as well as brief details on the solution strategy are addressed in Section 3. The manuscript is concluded in Section 4.

Notation Throughout the work at hand, a direct tensor notation is used. Scalars are written as a, vectors as $\boldsymbol{a}$, tensors of second order as $\boldsymbol{A}$ and tensors of fourth order as $\mathbb{A}$. The scalar product between two tensors is written as $\boldsymbol{a} \cdot \boldsymbol{b}$, $\boldsymbol{A} \cdot \boldsymbol{B}$, and $\mathbb{A} \cdot \mathbb{B}$. The linear mapping of a vector by a tensor of 2nd order is written as $\boldsymbol{A}\boldsymbol{b}$, and of the mapping of a 2nd order tensor by a 4th order tensor as $\mathbb{A}[\boldsymbol{B}]$. A composition between two tensors of 2nd or 4th order is written as $\boldsymbol{A}\boldsymbol{B}$ or $\mathbb{A}\mathbb{B}$, respectively. The dyadic product between two vectors or two tensors, e.g., of 2nd order is written as $\boldsymbol{a} \otimes \boldsymbol{b}$, respectively, $\boldsymbol{A} \otimes \boldsymbol{B}$. The material time derivative of field a of arbitrary tensorial order is written as $\dot{a}$.

2 Revisiting thermomechanically coupled and weakly coupled theory, and multiphase-field method

Motivation and subsequent procedure For the simulation of microstructure mechanics without phase transformations the TWT is commonly applied in the small strain regime. This is justified by the negligible heating due to deformation associated with small strains and small (plastic) strain rates. The present work shows that this justification does not apply to simulations that take into account phase transformations, which are commonly performed in the context of the MPFM. The impact of using TCT instead of TWT is discussed in this context. In this section, the concept of the TCT and TWT is revisited. To illustrate the relation and differences between both the underlying assumptions are provided. Moreover, the fundamentals of the considered MPFM are discussed.

2.1 Fundamentals

Energy balance Regarding a classical Cauchy–Boltzmann continuum, the balance of total energy for a material volume $\mathcal{V}_t$ with respect to the current configuration at time t is given by

$$\frac{\mathrm{d}}{\mathrm{d}t}\int_{\mathcal{V}_t} \rho\left(e + \frac{1}{2}\boldsymbol{v}\cdot\boldsymbol{v}\right)\,\mathrm{d}v = \int_{\mathcal{V}_t} \rho\,(\boldsymbol{b}\cdot\boldsymbol{v} + r)\,\mathrm{d}v + \int_{\partial\mathcal{V}_t} (\boldsymbol{t}\cdot\boldsymbol{v} + h)\,\mathrm{d}a, \tag{1}$$

with the mass density ρ, the specific free energy e, the velocity field $\boldsymbol{v}$, the body force $\boldsymbol{b}$, the specific heat supply r, the traction vector $\boldsymbol{t}$ and the heat flux h, cf., e.g., [57, p.148].

Balance equations The invariance of the balance of total energy with respect to a change of observer yields the Cauchy stress tensor $\boldsymbol{\sigma}$ and the heat flux vector $\boldsymbol{q}$

$$\boldsymbol{t} = \boldsymbol{\sigma}\boldsymbol{n}, \quad \text{and} \quad h = -\boldsymbol{q}\cdot\boldsymbol{n}, \tag{2}$$

as well as the balance of mass, linear and angular momentum

$$\dot{\rho} + \rho\,\mathrm{div}\,(\boldsymbol{v}) = 0, \quad \rho\boldsymbol{a} = \mathrm{div}\,(\boldsymbol{\sigma}) + \rho\boldsymbol{b}, \quad \boldsymbol{\sigma} = \boldsymbol{\sigma}^{\mathsf{T}}, \tag{3}$$

cf., e.g., [57]. Herein, $\boldsymbol{n}$ denotes the outward pointing normal vector on $\partial\mathcal{V}_t$ and $\boldsymbol{a} = \dot{\boldsymbol{v}}$ the acceleration field. A detailed discussion with respect to regular and singular points, respectively, regarding an extended continuum is provided, e.g., by Prahs and Böhlke [58,59]. Taking into account Eqs. (2) and (3), the localization of Eq. (1) yields the balance of internal energy, reading

$$\rho\dot{e} = \rho r + \boldsymbol{\sigma}\cdot\boldsymbol{D} - \mathrm{div}\,(\boldsymbol{q}), \tag{4}$$

where $\boldsymbol{D}$ denotes the symmetric part of the velocity gradient. Subsequently, the following assumption is considered

A1 A small deformation theory is considered, implying a constant mass density, as well as small strains, i.e., $\boldsymbol{D} = \dot{\boldsymbol{\varepsilon}}$, holds true cf., e.g., [60, pp. 30–32].

2.2 Thermomechanically coupled theory

Exploitation of the Clausius–Duhem inequality In the following, the Clausius–Duhem inequality is considered, as a special form of the dissipation inequality, based on the following assumptions

A2 The entropy flux is given constitutively by $\boldsymbol{q}/\theta$.

A3 The entropy supply in regular points is given constitutively by $\rho r/\theta$.

Consequently, the Clausius–Duhem inequality is given by

$$\rho\delta = \rho\theta\dot{\eta} - \rho r + \theta\mathrm{div}\left(\frac{\boldsymbol{q}}{\theta}\right) \geq 0, \tag{5}$$

where δ denotes the specific dissipation, η the mass specific entropy, and θ the absolute temperature cf., e.g., [61, Eq. (3.1)]. Accounting for $\boldsymbol{g} = \mathrm{grad}\,(\theta)$ as well as the Legendre transformation $\psi = e - \theta\eta$, cf., e,g., [62], and taking into account Eq. (4), Eq. (5) reads

$$\rho\delta = \boldsymbol{\sigma}\cdot\dot{\boldsymbol{\varepsilon}} - \rho\dot{\psi} - \rho\dot{\theta}\eta - \frac{1}{\theta}\boldsymbol{q}\cdot\boldsymbol{g} \geq 0, \tag{6}$$

with the specific free energy ψ. In the context of a TCT, the following assumptions are considered

A4 The small strain tensor $\boldsymbol{\varepsilon}$ is additively decomposed into an elastic $\boldsymbol{\varepsilon}^{\mathrm{e}}$, a plastic $\boldsymbol{\varepsilon}^{\mathrm{p}}$ and a thermal contribution $\boldsymbol{\alpha}\Delta\theta$, as well as a contribution due to an eigenstrain $\boldsymbol{\varepsilon}^{*}$, reading

$$\boldsymbol{\varepsilon} = \boldsymbol{\varepsilon}^{\mathrm{e}} + \boldsymbol{\varepsilon}^{\mathrm{p}} + \boldsymbol{\alpha}\Delta\theta + \boldsymbol{\varepsilon}^{*}. \tag{7}$$

Here, $\Delta\theta = \theta - \theta_0$ is considered with the referential temperature θ_0, and $\boldsymbol{\alpha}$ denotes the thermal expansion tensor.

A5 The specific free energy depends on the total strain $\boldsymbol{\varepsilon}$, the plastic strain $\boldsymbol{\varepsilon}^{\mathrm{p}}$, the eigenstrain $\boldsymbol{\varepsilon}^{*}$, and the temperature θ, reading

$$\psi = \psi(\boldsymbol{\varepsilon}, \boldsymbol{\varepsilon}^{\mathrm{p}}, \boldsymbol{\varepsilon}^{*}, \theta). \tag{8}$$

A6 The eigenstrain $\boldsymbol{\varepsilon}^{*}$ is constant, i.e., $\dot{\boldsymbol{\varepsilon}}^{*} = 0$ holds true.

Accounting for Eq. (8), Eq. (6) reads

$$\left(\boldsymbol{\sigma} - \rho\frac{\partial\psi}{\partial\boldsymbol{\varepsilon}}\right)\cdot\dot{\boldsymbol{\varepsilon}} - \rho\frac{\partial\psi}{\partial\boldsymbol{\varepsilon}^{\mathrm{p}}}\cdot\dot{\boldsymbol{\varepsilon}}^{\mathrm{p}} - \rho\left(\eta + \frac{\partial\psi}{\partial\theta}\right)\cdot\dot{\theta} - \frac{1}{\theta}\boldsymbol{q}\cdot\boldsymbol{g} \geq 0. \tag{9}$$

Following the Coleman–Noll procedure, cf., e.g., [61], exploiting Eq. (9) yields the potential relations for the Cauchy stress and the entropy

$$\boldsymbol{\sigma} = \rho\frac{\partial\psi}{\partial\boldsymbol{\varepsilon}}, \quad \eta = -\frac{\partial\psi}{\partial\theta}. \tag{10}$$

With respect to the TCT, the following assumption is considered

A7 The specific free energy reads

$$\begin{aligned}\psi =& \frac{1}{2\rho}\left(\boldsymbol{\varepsilon} - \boldsymbol{\varepsilon}^{\mathrm{p}} - \alpha\Delta\theta\boldsymbol{I} - \boldsymbol{\varepsilon}^{*}\right)\cdot\left(\mathbb{C}\left[\boldsymbol{\varepsilon} - \boldsymbol{\varepsilon}^{\mathrm{p}} - \alpha\Delta\theta\boldsymbol{I} - \boldsymbol{\varepsilon}^{*}\right]\right)\\ &- \frac{1}{2\rho}(\alpha\Delta\theta\boldsymbol{I})\cdot(\alpha\Delta\theta\boldsymbol{I}) - \kappa_c\left(\theta\ln\frac{\theta}{\theta_0} - \Delta\theta\right),\end{aligned} \tag{11}$$

where $\mathbb{C}$ denotes the stiffness tensor, α the scalar-valued coefficient of thermal expansion, $\boldsymbol{I}$ the identity tensor of second order, accounting for an isotropic thermal expansion, and κ_c the heat capacity, cf., e.g., [63]. This choice of the specific free energy exhibits a coupling of the mechanical and thermal contributions, such that the interactions between the balance of linear momentum and heat conduction are accounted for. Thus, the TCT is contrary to the assumptions and consequences of a purely mechanical theory as discussed in [64].

Regarding the Cauchy stress,

$$\boldsymbol{\sigma} = \mathbb{C}\left[\boldsymbol{\varepsilon} - \boldsymbol{\varepsilon}^{\mathrm{p}} - \alpha\Delta\theta\boldsymbol{I} - \boldsymbol{\varepsilon}^{*}\right], \quad \rho\frac{\partial\psi}{\partial\boldsymbol{\varepsilon}^{\mathrm{p}}} = -\boldsymbol{\sigma} \tag{12}$$

hold true. Thus, the dissipation inequality according to Eq. (6) can be written in a simplified reduced form, as

$$\boldsymbol{\sigma}\cdot\dot{\boldsymbol{\varepsilon}}^{\mathrm{p}} - \frac{1}{\theta}\boldsymbol{q}\cdot\boldsymbol{g} \geq 0. \tag{13}$$

This reduced dissipation inequality can be fulfilled by considering Fourier's law as $\boldsymbol{q} = -\boldsymbol{\kappa} \boldsymbol{g}$, with the positive definite heat conduction tensor $\boldsymbol{\kappa}$, as well as Mises plasticity with an associative flow rule, cf., e.g., [65, p.83], reading

$$f = ||\mathrm{dev}\,(\boldsymbol{\sigma})|| - \sqrt{\frac{2}{3}}\sigma_{\mathrm{Y}} \leq 0, \quad \dot{\boldsymbol{\varepsilon}}^{\mathrm{p}} = \gamma \frac{\partial f}{\partial \mathrm{dev}\,(\boldsymbol{\sigma})} = \gamma \frac{\mathrm{dev}\,(\boldsymbol{\sigma})}{||\mathrm{dev}\,(\boldsymbol{\sigma})||}, \quad \gamma \geq 0, \tag{14}$$

leading to

$$\gamma ||\mathrm{dev}\,(\boldsymbol{\sigma})|| + \frac{1}{\theta} \boldsymbol{g} \cdot (\boldsymbol{\kappa} \boldsymbol{g}) \geq 0. \tag{15}$$

The consistency parameter is referred to as γ, the initial yield stress as σ_{Y}, and the deviator of the Cauchy stress as $\mathrm{dev}\,(\boldsymbol{\sigma})$. In the work at hand, an elastic perfectly plastic material behavior is considered, cf., e.g., [1, Fig. 3.28]. Thus, hardening is neglected and σ_{Y} is just referred as yield stress, for brevity.

Heat conduction After a brief auxiliary calculation, provided in the Appendix, and the introduction of the heat capacity for constant strains

$$c_{\varepsilon} = -\theta \frac{\partial^2 \psi}{\partial \theta^2} \tag{16}$$

similar to Lemaitre and Chaboche [1, p.67], reformulation of Eq. (4) reads

$$\rho c_{\varepsilon} \dot{\theta} = \rho r - \mathrm{div}\,(\boldsymbol{q}) + \boldsymbol{\sigma} \cdot \dot{\boldsymbol{\varepsilon}}^{\mathrm{p}} + \theta \frac{\partial \boldsymbol{\sigma}}{\partial \theta} \cdot \dot{\boldsymbol{\varepsilon}} - \theta \frac{\partial \boldsymbol{\sigma}}{\partial \theta} \cdot \dot{\boldsymbol{\varepsilon}}^{\mathrm{p}}. \tag{17}$$

Due to the second term of the specific free energy according to Eq. (11), the heat capacity is constant at constant strains and, thereby, $c_{\varepsilon} = \kappa_c$ holds true. Regarding the thermal material parameters, the following assumptions are considered, for simplicity

A8 The heat conduction is isotropic, i.e., $\boldsymbol{q} = -\kappa \boldsymbol{g}$ holds true, where the coefficient κ is considered to be constant.

A9 The heat supply is neglected, i.e., $r = 0$ holds true.

Introducing the Laplacian $\triangle(\cdot)$ and taking into account Eq. (12), Eq. (17) reads

$$\rho \kappa_c \dot{\theta} = \kappa \triangle(\theta) + \boldsymbol{\sigma} \cdot \dot{\boldsymbol{\varepsilon}}^{\mathrm{p}} - \theta \alpha\, (\mathbb{C}[\boldsymbol{I}]) \cdot \left(\dot{\boldsymbol{\varepsilon}} - \dot{\boldsymbol{\varepsilon}}^{\mathrm{p}}\right), \tag{18}$$

Lemaitre and Chaboche [1, p.67]. Regarding the elastic material behavior, the following assumption is considered, for simplicity

A10 An isotropic elastic material behavior is considered with the stiffness $\mathbb{C} = 3K\mathbb{P}_1 + 2G\mathbb{P}_2$ with the compression modulus K, the shear modulus G, as well as the first and second projector $\mathbb{P}_1 = 1/3\boldsymbol{I} \otimes \boldsymbol{I}$, $\mathbb{P}_2 = \mathbb{I}^{\mathrm{S}} - \mathbb{P}_1$. Thus, $\mathbb{C}[\boldsymbol{I}] = 3K\boldsymbol{I}$ holds true.

Moreover, taking into account the plastic strain rate according to Eq. $(14)_2$ and the linearity of the trace-operator, cf., e.g., [66, p.14], $\boldsymbol{\sigma} \cdot \dot{\boldsymbol{\varepsilon}}^{\mathrm{p}} = \gamma ||\mathrm{dev}\,(\boldsymbol{\sigma})||$ and $\mathrm{tr}\,(\dot{\boldsymbol{\varepsilon}}^{\mathrm{p}}) = 0$ hold true, and Eq. (18) reads

$$\rho \kappa_c \dot{\theta} = \kappa \triangle(\theta) + \gamma ||\mathrm{dev}\,(\boldsymbol{\sigma})|| + p_{\mathrm{thm}}, \quad p_{\mathrm{thm}} := -3K\alpha\theta\, \mathrm{tr}\,(\dot{\boldsymbol{\varepsilon}}), \tag{19}$$

with $\mathrm{tr}\,(\cdot)$ denoting the trace of a second order tensor. Subsequently, the term $p_{\mathrm{thm}} = -3K\alpha\theta\, \mathrm{tr}\,(\dot{\boldsymbol{\varepsilon}})$ is referred to as thermomechanical coupling contribution and $\boldsymbol{\sigma} \cdot \dot{\boldsymbol{\varepsilon}}^{\mathrm{p}}$, respectively $\gamma ||\mathrm{dev}\,(\boldsymbol{\sigma})||$, as plastic stress power density.

2.3 Thermomechanically weakly coupled theory

Exploitation of the Clausius–Duhem inequality In contrast to the TCT, assumptions A4, A5, and A7 are modified. However, a constant eigenstrain according to A6 is considered also within the TWT. Thus, regarding the TWT, the following assumptions are considered

A11 The small strain tensor is additively decomposed into an elastic $\boldsymbol{\varepsilon}^{\mathrm{e}}$ and a plastic $\boldsymbol{\varepsilon}^{\mathrm{p}}$ contribution, as well as a contribution due to an eigenstrain $\boldsymbol{\varepsilon}^{*}$, reading

$$\boldsymbol{\varepsilon} = \boldsymbol{\varepsilon}^{\mathrm{e}} + \boldsymbol{\varepsilon}^{\mathrm{p}} + \boldsymbol{\varepsilon}^{*}. \tag{20}$$

Consequently, no thermal strains are considered.

A12 An additive decomposition of the specific free energy into a purely mechanical and a purely thermal contribution is considered, reading

$$\psi = \psi_{\mathrm{m}} + \psi_{\theta}, \quad \psi_{\mathrm{m}} \neq \psi_{\mathrm{m}}(\theta), \quad \psi_{\theta} = \psi_{\theta}(\theta). \tag{21}$$

A13 The considered contributions of the specific free energy for the TWT read

$$\psi_{\mathrm{m}} = \frac{1}{2\rho} \left(\boldsymbol{\varepsilon} - \boldsymbol{\varepsilon}^{\mathrm{p}} - \boldsymbol{\varepsilon}^{*}\right) \cdot \left(\mathbb{C}\left[\boldsymbol{\varepsilon} - \boldsymbol{\varepsilon}^{\mathrm{p}} - \boldsymbol{\varepsilon}^{*}\right]\right), \quad \psi_{\theta} = -\kappa_c \left(\theta \ln \frac{\theta}{\theta_0} - \Delta\theta\right). \tag{22}$$

As a consequence of A12, the potential relations for the stress and the entropy according to Eq. (10) are modified, reading

$$\boldsymbol{\sigma} = \rho \frac{\partial \psi_{\mathrm{m}}}{\partial \boldsymbol{\varepsilon}}, \quad \eta = -\frac{\partial \psi_{\theta}}{\partial \theta}. \tag{23}$$

Due to A13, the Cauchy stress tensor is given by

$$\boldsymbol{\sigma} = \mathbb{C}\left[\boldsymbol{\varepsilon} - \boldsymbol{\varepsilon}^{\mathrm{p}} - \boldsymbol{\varepsilon}^{*}\right]. \tag{24}$$

The results according to Eqs. $(12)_2$ to (14) are not affected and, thus, the same as for the TCT.

Heat conduction Based on Eq. $(23)_2$, the rate of the entropy is given by

$$\dot{\eta} = \left(-\frac{\partial \psi_{\theta}}{\partial \theta}\right)^{\cdot} = -\frac{\partial \dot{\psi}_{\theta}}{\partial \theta} = -\frac{\partial^2 \dot{\psi}_{\theta}}{\partial \theta^2} \dot{\theta}. \tag{25}$$

Thus, in contrast to Eq. (48), no coupling terms enter the rate of entropy regarding the TWT, and the contribution associated with the derivative $\partial \boldsymbol{\sigma} / \partial \theta$ is omitted in Eq. (18). The heat capacity at constant strains is introduced as in Eq. (16). Regarding the TWT, the choice of the specific free energy according to A13 ensures a constant heat capacity at constant strains. Accounting for the definition of the plastic strain rate, given by Eq. $(14)_2$, the equation of heat conduction is given by

$$\rho \kappa_c \dot{\theta} = \kappa \triangle(\theta) + \gamma ||\mathrm{dev}\,(\boldsymbol{\sigma})||. \tag{26}$$

Compared to the TCT, the equation of heat conduction according to Eq. (26) is simplified and accounts only for the plastic stress power density, however not for the thermomechanical coupling contribution p_{thm}.

Comparison between TCT and TWT For a better comparison, Hooke's law as well as the equation of heat conduction, obtained for TCT and TWT, respectively, are compared, regarding an isotropic elastic and thermal material behavior and under consideration of Mises plasticity without hardening, in Table 1. Regarding the TCT, the stresses are affected by thermal strains, and both the plastic stress power density $\gamma ||\mathrm{dev}\,(\boldsymbol{\sigma})||$ as well as the thermomechanical coupling contribution p_{thm} affect the heat conduction. While the first always acts as a heat source, the latter acts as heat source or heat sink, respectively. In contrast, no thermal strain is accounted for by A11, and p_{thm} vanishes with respect to the heat conduction equation, for the TWT theory. Consequently, the balance of linear momentum is not affected by any thermal contribution in case of the TWT. It has to be stressed that

- The combination of Hooke's law of the TCT with the heat conduction of the TWT is thermodynamically not admissible: In accordance with the additive decomposition of the strain tensor, cf. Eq. (7), the elastic contribution of the specific free energy has to depend on the thermal strains, cf. Eq. (11), yielding the thermomechanical coupling contribution $p_{\mathrm{thm}} = -3K\alpha\theta\, \mathrm{tr}\,(\dot{\boldsymbol{\varepsilon}})$.

.

Table 1
Comparison of Hooke's law and the equation of heat conduction for both the TCT and the TWT, considering both isotropic elastic and thermal material properties. While the stress power $\gamma||\mathrm{dev}\,(\boldsymbol{\sigma})||$ is present for both the TCT and the TWT, the thermomechanical coupling contribution $p_{\mathrm{thm}} = -3K\alpha\theta\ \mathrm{tr}\,(\dot{\boldsymbol{\varepsilon}})$ is only accounted for by the TCT. In case of a vanishing coefficient of thermal expansion, TCT and TWT coincide. The combination of Hooke's law of the TCT with the heat conduction of the TWT, and vice versa, is thermodynamically not consistent.

	Hooke's law	Equation of heat conduction
TCT	$\boldsymbol{\sigma} = \mathbb{C}\,[\boldsymbol{\varepsilon} - \boldsymbol{\varepsilon}^{\mathrm{p}} - \alpha\Delta\theta\boldsymbol{I} - \boldsymbol{\varepsilon}^{*}]$	$\rho\kappa_c\dot{\theta} = \kappa \triangle(\theta) + \gamma\|\|\mathrm{dev}\,(\boldsymbol{\sigma})\|\| - 3K\alpha\theta\ \mathrm{tr}\,(\dot{\boldsymbol{\varepsilon}})$
TWT	$\boldsymbol{\sigma} = \mathbb{C}\,[\boldsymbol{\varepsilon} - \boldsymbol{\varepsilon}^{\mathrm{p}} - \boldsymbol{\varepsilon}^{*}]$	$\rho\kappa_c\dot{\theta} = \kappa \triangle(\theta) + \gamma\|\|\mathrm{dev}\,(\boldsymbol{\sigma})\|\|$

- The combination of Hooke's law of the TWT with the heat conduction of the TCT is also not admissible: The additive decomposition of the strain according to Eq. (20) does not allow for a dependency of the elastic contribution of the specific free energy, and thereby, Hooke's law, on the thermal strain, cf. Eq. (22).
- For a negligibly small or vanishing coefficient of thermal expansion, TCT and TWT coincide.

2.4 Evolution of inclusion modeled by multiphase-field method

Considered free energy functional In this work, the multiphase-field method (MPFM), cf., e.g., [12–14,67], is used to model the evolution of the respective phases. In this context, the considered free energy functional reads

$$\mathcal{F}\left[\boldsymbol{\phi}, \mathrm{grad}\,(\boldsymbol{\phi}), \boldsymbol{u}\right] = \int_{\mathcal{V}_t} f\,\mathrm{d}v, \tag{27}$$

cf., e.g., [68]. Here, the free energy functional is referred to as $\mathcal{F}$, the free energy density as f and the displacement field as $\boldsymbol{u}$. Considering problems with a total number of N phases, the n-tuple of order parameters is denoted as $\boldsymbol{\phi} = \{\phi_1, \ldots, \phi_N\}$ and the n-tuple of the corresponding gradients as $\mathrm{grad}\,(\boldsymbol{\phi})$. The order parameters are subject to the summation constraint

$$\forall \boldsymbol{x} \in \mathcal{V}_t,\ t \geq 0: \quad \sum_{\alpha=1}^{N} \phi_\alpha(\boldsymbol{x}, t) = 1, \tag{28}$$

cf., e.g., [14, p.2]. Thus, the order parameter ϕ_α can be seen as a local volume fraction of phase α. Subsequently, the following assumptions are considered with respect to the free energy density used within the MPFM.

A14 An additive decomposition of the free energy density is considered, reading

$$f = f_{\mathrm{grad}} + f_{\mathrm{pot}} + \overline{f}_{\mathrm{bulk}}. \tag{29}$$

While the contribution $\overline{f}_{\mathrm{bulk}}$ accounts for the specific free energy of the bulk material, the contributions f_{grad} and f_{pot} are due to the regularization of a sharp interface within the MPFM.

A15 According to the model of Steinbach and Pezzolla [13], the contribution f_{grad} is given by

$$f_{\mathrm{grad}}\,(\boldsymbol{\phi}, \mathrm{grad}\,(\boldsymbol{\phi})) = \epsilon \sum_{\beta=2}^{N} \sum_{\alpha=1}^{\beta-1} \gamma_{\alpha\beta}\ \mathrm{grad}\left(\phi_\alpha\right) \cdot \mathrm{grad}\left(\phi_\beta\right) \tag{30}$$

and the contribution f_{pot} is expressed by means of the multi-obstacle potential, cf., e.g., [14], as

$$f_{\mathrm{pot}}\,(\boldsymbol{\phi}) = \frac{16}{\epsilon\pi^2} \sum_{\beta=2}^{N} \sum_{\alpha=1}^{\beta-1} \gamma_{\alpha\beta}\ \phi_\alpha\phi_\beta. \tag{31}$$

In this context, $\gamma_{\alpha\beta}$ refers to the interfacial energy between phase α and β. The parameter ϵ determines the width of the interface. For diffuse interfaces in equilibrium state, its width is obtained by $\pi^2\epsilon/4$, cf., e.g., [69]. Furthermore, f_{grad} and f_{pot} are balanced and their sum can be viewed as a regularized surface Dirac distribution multiplied by the interfacial energy $\gamma_{\alpha\beta}$.

A16 The contribution $\overline{f}_{\mathrm{bulk}}$ is obtained by the interpolation

$$\overline{f}_{\mathrm{bulk}} = \sum_{\alpha=1}^{N} \phi_\alpha \rho_\alpha \psi_\alpha \tag{32}$$

of the phase-inherent bulk energies, where ψ_α refers to the specific free energy according to Eq. (11) or Eq. (22), respectively, with respect to phase α.

Governing equations The minimization of Eq. (27) with respect to $\boldsymbol{u}$ yields the balance of linear momentum for the diffuse interface region, reading

$$\mathrm{div}\,(\overline{\boldsymbol{\sigma}}) = \boldsymbol{0}, \quad \overline{\boldsymbol{\sigma}} = \sum_{\alpha=1}^{N} \phi_\alpha \boldsymbol{\sigma}^\alpha, \tag{33}$$

where $\overline{\boldsymbol{\sigma}}$ is an interpolated stress. The phase-inherent stresses $\boldsymbol{\sigma}^\alpha$ are in general unknown within the diffuse interface region and need to be determined by a diffuse interface approximation. They can be obtained, e.g., from an effective stiffness tensor resulting from a linear interpolation of the phase-inherent stiffness tensors, which yields a diffuse interface approximation according to the model of Khachaturyan [70]. In contrast, the enhanced approach according to Schneider et al. [71] is employed, here, which meets both the Hadamard condition and the balance of linear momentum on a singular surface. Both conditions are enforced at each point of the diffuse interface by means of the corresponding phase-inherent quantities. More details of the approach are provided by Schneider et al. [71]. Regarding phase α, the evolution equation is given by

$$\frac{\partial\phi_\alpha}{\partial t} = -\frac{1}{\epsilon\tilde{N}} \sum_{\substack{\beta=1 \\ \beta\neq\alpha}}^{\tilde{N}} M_{\alpha\beta} \left(\frac{\delta f}{\delta\phi_\alpha} - \frac{\delta f}{\delta\phi_\beta} \right). \tag{34}$$

Here, the mobility of the diffuse interface between two phases α and β is referred to as $M_{\alpha\beta}$. Therefore, a different speed of phase transformation can be provided for each specific phase pairing. The mobility parameter $M_{\alpha\beta}$ globally scales the temporal change of order parameters between two phases. Thus, it determines the kinetics of the overall phase transformation of a phase pair α and β. Local differences in interface velocities, arising from phase transformation, are caused by differences in the phase-inherent free energy densities $\psi_\alpha(\boldsymbol{x}, t)$. In the present work, they are introduced by elastic contributions of $\psi_\alpha(\boldsymbol{x}, t)$ according to Eq. (32) and, thus, the local interface velocity is space and time dependent. The number of locally present phases is denoted by $\tilde{N}$, which is defined as

$$\tilde{N}(\boldsymbol{x}, t) = \sum_{\alpha=1}^{N} \mathrm{H}(\phi_\alpha), \tag{35}$$

where H denotes the Heaviside function. The considered variational derivative is defined as

$$\frac{\delta f}{\delta\phi_\alpha} := \left(\frac{\partial f}{\partial\phi_\alpha} - \mathrm{div}\left(\frac{\partial f}{\partial\,\mathrm{grad}\,(\phi_\alpha)} \right) \right), \tag{36}$$

cf., e.g., [72, Eqs. (13.63) & (13.64)]. In addition, the boundary condition on the Neumann boundary $\partial\mathcal{V}_t^{\mathrm{N}}$, given by

$$\frac{\partial f_{\mathrm{grad}}}{\partial\,\mathrm{grad}\,(\phi_\alpha)} \cdot \boldsymbol{n} = 0, \quad \forall \boldsymbol{x} \in \partial\mathcal{V}_t^{\mathrm{N}}, \tag{37}$$

has to be fulfilled.

Phase-inherent plasticity In the context of MPFM, different implementations of the plastic material behavior within the diffuse interface region are known in literature. Here, the so-called phase-inherent plasticity is considered, i.e., each phase exhibits its own plastic fields and its own flow rule in form of Eq. (14). The material parameters are not

interpolated within the diffuse interface. A detailed description on the phase-inherent treatment of plasticity in the MPFM context is given by Herrmann et al. [68]. Using the phase-inherent approach to plasticity according to Herrmann et al. [68], no inheritance of plastic fields is considered, cf., e.g., [73]. Thus, if a phase exhibits plastic strains and transforms to another phase, the previously present plastic strains vanish due to the transformation. While it is possible to account for inheritance of plastic fields within the phase-inherent approach, it is not accounted for, here, for brevity.

Thermal driving forces In the work at hand, the thermal material properties κ_c, κ, and α are considered to be the same, for simplicity, cf. Table 2. Thus, no additional contributions in terms of thermal driving forces have to be considered. However, in the more general case, thermal driving forces due to different thermal parameters have to be taken into account. The present work focuses on discussing the difference between the TCT and TWT and, thereby, the effect of the thermomechanical coupling regarding inclusion growth due to different yield stresses. Effects due to a contrast in the thermal properties are, therefore, not discussed.

3 Model application in numerical simulations

Motivation and subsequent procedure This section discusses the effect of using a TCT as opposed to a TWT with respect to the growth of an elastoplastic inclusion, subjected to a distortion, within an elastoplastic matrix under load. To this end, the boundary value problem and the solution procedure are briefly stated. The effect of using a TCT in contrast to a TWT is discussed in terms of the growth kinetics of the inclusion and its shape. The special case of a vanishing heat conduction is addressed, since the temperature distribution can be additively decomposed into the accumulation due to the thermomechanical coupling contribution and the plastcic stress power, respectively.

3.1 Boundary conditions and considered parameters

Considered instructive trivial form As an application example, we consider a simplified martensitic phase transformation of a spherical inclusion, subjected to transversely isotropic eigenstrains, inside an austenitic matrix under external load. The difference in mass density between matrix and inclusion is modeled via eigenstrains within the inclusion. They lead to plastic deformation in the weaker matrix material and thus the resulting energy difference induces phase transformation according to the Greenwood–Johnson effect, cf. [34]. Numerical simulations are conducted employing both the TWT and TCT.

Boundary condition In the following, a composite consisting of an elastoplastic, spherical inclusion in an elastoplastic matrix is considered. The inclusion is subjected to eigenstrains $\boldsymbol{\varepsilon}^*$, with

$$\varepsilon^*_{xx} = \varepsilon^*_{yy} = \varepsilon^* \in \{0.001, 0.005, 0.01\}, \quad \varepsilon^*_{zz} = \varepsilon^*_{xy} = \varepsilon^*_{xz} = \varepsilon^*_{yz} = 0. \tag{38}$$

The matrix as well as the inclusion exhibit the same elastic material behavior. The yield stress of the inclusion is higher than the yield stress of the matrix. This set of parameters mimics austenite and martensite, respectively. Fig. 1 represents the boundary conditions applied. A plane strain setup is considered employing the Neumann boundary conditions

$$\bar{\boldsymbol{t}}(L/2, y, z) = \sigma_0 \boldsymbol{e}_x, \quad \bar{\boldsymbol{t}}(-L/2, y, z) = -\sigma_0 \boldsymbol{e}_x,$$
$$\bar{\boldsymbol{t}}(x, L/2, z) = \bar{\boldsymbol{t}}(x, -L/2, z) = \boldsymbol{0}, \tag{39}$$

with $\sigma_0 = 100\,\mathrm{MPa}$, and the Dirichlet boundary conditions

$$u_z(x, y, B/2) = u_z(x, y, -B/2) = 0. \tag{40}$$

Here, the width and height of the considered simulation domain is referred to as L, and the thickness as B. The domain length is chosen as $L = 25 d_0$, where d_0 denotes the initial inclusion diameter. Moreover, at all boundaries, a vanishing normal heat flux is prescribed, reading

$$\boldsymbol{q} \cdot \boldsymbol{n} = 0 \quad \forall \boldsymbol{x} \in \partial \mathcal{V}_t. \tag{41}$$

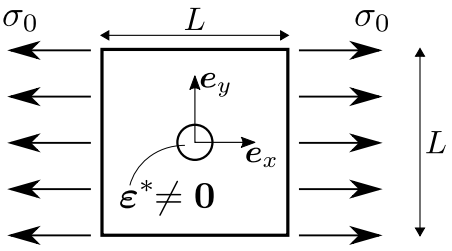

Fig. 1. Illustration of considered boundary value problem for discussing the difference between the use of TCT and TWT on the inclusion growth. Specifically, the transformation-induced growth of an elastoplastic inclusion, subjected to a distortion, within an elastoplastic matrix under load is considered. The distortion is realized by transversely isotropic eigenstrains, i.e., $\varepsilon^*_{xx} = \varepsilon^*_{yy} = \varepsilon^*$ and $\varepsilon^*_{zz} = \varepsilon^*_{xy} = \varepsilon^*_{xz} = \varepsilon^*_{yz} = 0$ are considered with respect to the Cartesian coordinate system. Moreover, a plane strain setup is applied with non-vanishing Neumann boundary conditions at the left and the right side of the matrix in $\boldsymbol{e}_x$-direction.

Material and geometrical parameters considered The material behavior is considered to be elastic and perfectly plastic, i.e., hardening is not considered, with isotropic elasticity, cf., e.g., [1, p. 104]. The parameters associated with the TCT and TWT discussed above and used for the simulations discussed subsequently are listed in Table 2. The only difference between the material behavior of inclusion and matrix is the yield stress σ_Y, which is significantly higher for the inclusion. The inclusion is considered on a microscale with an initial diameter $d_0 = 20\,\mu\mathrm{m}$.

Numerical setup and solving procedure The considered partial differential equations (PDEs) are discretized on an equidistant Cartesian grid with the step size h_d being constant in all directions. The computations are carried out employing the in-house code Pace3D, cf. [74]. A number of 750×750 cells is used for discretization. The temperature equation as well as the momentum balance are solved implicitly employing a finite element discretization with linear elements. For the phase-field evolution an explicit time integration is used. All PDEs are solved by a staggered scheme in time, such that the coupling is treated explicitly, cf. Fig. 2. The coupling terms of the temperature equation are approximated with a trapezoidal rule, e.g., we use

$$\boldsymbol{\sigma} \cdot \dot{\boldsymbol{\varepsilon}}^\mathrm{p}(\boldsymbol{x}, t_n + \Delta t/2) \approx \frac{1}{2\Delta t} \left(\boldsymbol{\sigma}^{n+1} + \boldsymbol{\sigma}^n\right) \cdot \left((\boldsymbol{\varepsilon}^\mathrm{p})^{n+1} - (\boldsymbol{\varepsilon}^\mathrm{p})^n\right), \tag{42}$$

where n denotes the time step and Δt the time step size. Additionally, the simulations where conducted with a reduced resolution by factor 0.8 both in space and time. Similar results where observed, which indicates, that the chosen resolution is sufficient also with regard to the staggered coupling. The considered setup is a two-phase problem. Thus, the multiphase-field model simplifies due to $\phi_2 = 1 - \phi_1$, $\mathrm{grad}\,(\phi_2) = -\mathrm{grad}\,(\phi_1)$ arising from the summation constraint (28) in the two-phase case. With these simplifications, the evolution equation (34) yields

$$\frac{\partial \phi_1}{\partial t} = -M_{12}\gamma_{12}\left[\frac{16}{(\pi\epsilon)^2}(1 - 2\phi_1) - 2 \triangle (\phi_1)\right] + \frac{M_{12}}{\epsilon}\left(\rho_2\psi_2 - \rho_1\psi_1\right) \tag{43}$$

for phase 1. The distribution of the second phase is obtained from the summation constraint. For the simulations the parameter $\epsilon = 4/\pi^2\, 7 h_\mathrm{d}$ is considered, such that the width of the diffuse interface equals seven times the spatial discretization step size h_d. The characteristic time scale by means of the process end time t^end is 100 ns. A mobility $M_{12} = 1.4 \times 10^3\,\mathrm{m\,s\,kg^{-1}}$ is chosen, to achieve this time scale, which is typical for these transformation processes. The number of timesteps considered to reach the end time is 11 250. Additionally, the interfacial energy γ_{12} is chosen such, that the equilibrium profile for the phase-field is maintained during the simulation.

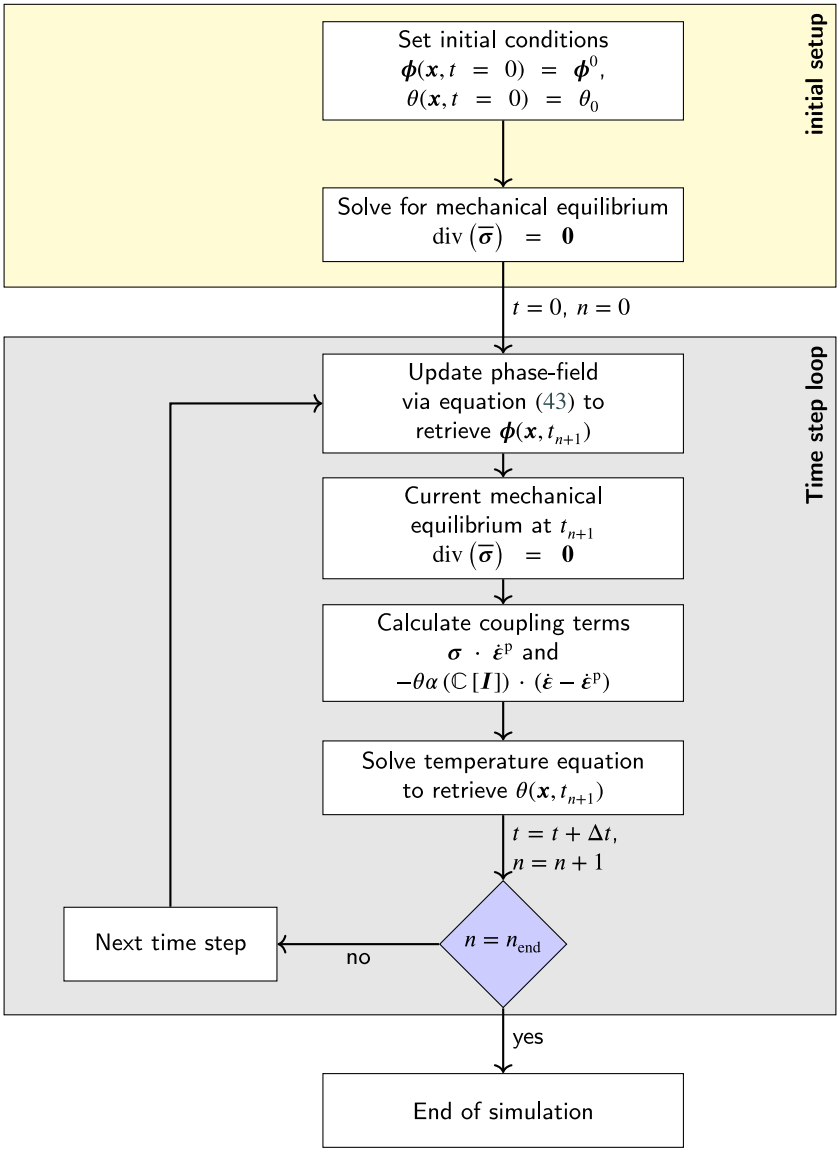

Fig. 2. Overview of the solution procedure for the considered model application. The equations for phase evolution (43), temperature (18) and the momentum balance (33) are coupled and solved with a staggered scheme. The phase-field is updated explicitly, the solution for mechanical equilibrium uses θ^n and $\boldsymbol{\phi}^{n+1}$. The coupling terms for temperature are integrated with the trapezoidal rule see e.g. Eq. (42).

Table 2
Considered parameters for an elastic and perfectly plastic (i.e., hardening is not considered) material behavior with isotropic elasticity: Young's modulus E, Poisson's ratio ν, mass density ρ, (initial) yield stress σ_{Y}, heat capacity at constant strains κ_c, coefficient of heat conduction κ, coefficient of thermal expansion α. The constitutive material behavior is intentionally kept as simple as possible. Here, the yield stress of the inclusion and matrix are the only parameters that differ.

Domain	E in GPa	ν in –	ρ in kg/m^3	σ_{Y} in MPa	κ_c in m^2/(s^2 K)	κ in kg m/(s^3 K)	α in 1/K
Inclusion	210	0.3	7800	1500	460	46	1×10^{-5}
Matrix	210	0.3	7800	250	460	46	1×10^{-5}

3.2 Comparison of simulation results for TCT and TWT

Comparison with respect to the growth of inclusion Regarding three different eigenstrains within the inclusion, the volume fraction of the inclusion over the simulation time is illustrated by Fig. 3. While the left diagram of Fig. 3 considers linear axes, the right diagram shows the same results with respect to double logarithmic axes. The dashed lines refer to the results obtained for the TWT, while the solid lines depict the results for the TCT. Regarding the double logarithmic diagram, the distributions can be approximated by straights with a similar slope over a certain range. The following observations can be made:

- TWT: The dashed lines can be approximated by straights with similar slope for $t/t^{\mathrm{end}} \in [0.1, 1]$ regarding the double logarithmic

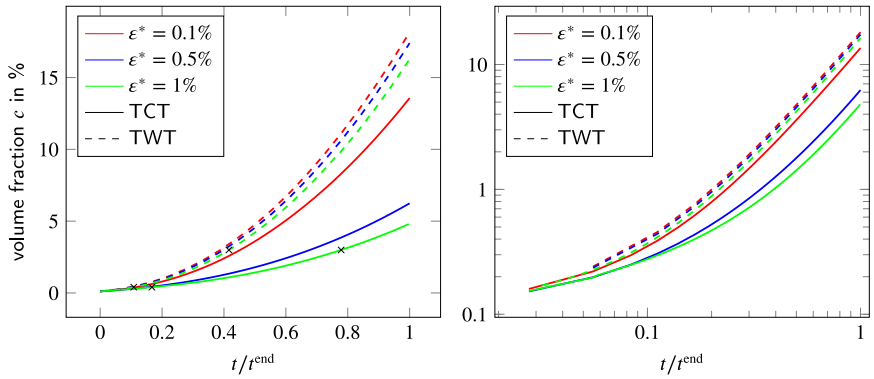

Fig. 3. Volume concentration over time for the growing inclusion. TWT: growth of inclusion illustrated by dashed lines, TCT: growth of inclusion illustrated by solid lines, black crosses: volume fractions $c = 0.4\%$ and $c = 3\%$ considered for the snapshots shown in Fig. 4 and 5. Left: linear scale of axes, right: double-logarithmic scale of axes.

Table 3
For the TCT the values of the half axes ratio $R_{yx} = S_y/S_x$ are compared to quantify the deviation from the spherical inclusion that is obtained by using TWT. In this context, S_x and S_y denote the length of the half-axes. The table lists the values of R_{yx} for two volume concentrations $c = 0.4\,\%$ and $c = 3\,\%$ and different amplitudes of the component ε^* of the eigenstrain $\boldsymbol{\varepsilon}^*$. Regarding a specific volume concentration, the value of R_{yx} increases for larger eigenstrains. For a specific eigenstrain, the increase of R_{yx} with respect to the increase of the volume concentration is even more pronounced.

ε^*	R_{yx} for $c = 0.4\%$	R_{yx} for $c = 3\%$
0.1%	0.99946	1.0014
0.5%	1.0387	1.1092
1.0%	1.0494	1.1414

diagram. Thus, the amplitude of the eigenstrain does not significantly influence the growth behavior of the inclusion. However, the distributions are shifted for a larger amplitude of eigenstrain. Thus, a larger eigenstrain leads to a smaller volume fraction of the inclusion.

- TCT: The distributions obtained in the context of TCT exhibit a significant shift compared to the distributions obtained for the TWT. For $t/t^{\text{end}} \in [0.3, 1]$ the distributions can be approximated by straights with similar slope regarding the double logarithmic diagram. Thus, also for TCT, the growth behavior is not significantly affected by the amplitude of the eigenstrains. Similar to the TWT, a larger amplitude of eigenstrain leads to a shift of the distributions, such that the larger the amplitude of the eigenstrain the smaller the volume concentration of the inclusion. This shift is more pronounced regarding the results for TCT than for TWT.
- The slopes of the approximative straights for TCT and TWT are approximately the same. Thus, the growth behavior of the inclusion for the TCT seems solely delayed compared with the TWT. Moreover, the TCT shows a higher sensitivity for a variation in the eigenstrains.

Finally, for a given simulation time, the TWT overestimates the growth of the inclusion compared to TCT, thereby affecting the effective material properties of the composite.

Comparison with respect to the accumulated plastic strain and shape of inclusion Regarding the two volume concentrations $c = 0.4\%$ and $c = 3\%$, illustrated by small cross markers in Fig. 3, the distribution of the accumulated plastic strain is depicted for the TWT and the TCT in Fig. 4. The following observations can be made:

- The shape of the distribution of the accumulated plastic strain $\epsilon_{\text{p,acc}}$ differs for the TWT and the TCT.
- For both TWT and TCT, the inclusion stays completely elastic throughout the simulation. This is ensured by using a phase-inherent plasticity without inheritance of plastic fields. Consequently, the accumulated plastic strain is vanishing within the inclusion and, thus, the shape of the inclusion is visible in Fig. 4.
- Regarding TWT, the shape of the inclusion stays spherical, whereas the shape becomes elliptic for TCT. To quantify the deviation from the spherical inclusion, obtained in TWT, the ratio $R_{yx} = S_y/S_x$ of the lengths of the half-axes of the inclusions are compared. Here, S_y and S_x refer to the length of the half-axis with respect to the y- and x-axis, respectively. Regarding the TCT, the values of R_{yx} are listed in Table 3. They increase both with larger eigenstrain and with increasing volume fraction of the inclusion. For $\varepsilon^* = 0.5\%$ and $\varepsilon^* = 1\%$, the inclusion height grows faster, than its width and this effect is more pronounced for larger eigenstrains. For $\varepsilon^* = 0.1\%$ the inclusion stays almost spherical. In the TWT case, $R_{yx} \approx 1$ is observed in all considered cases and thus, the inclusion stays spherical.
- The deviation of R_{yx} from 1, characterizing a spherical inclusion, can be associated with the heat conduction present in the composite. Regarding the TCT, the temperature distribution at $c = 0.4\%$ and $c = 3\%$ is depicted at the top of Fig. 5. The median of the diffuse interface, the transition region between inclusion and matrix, is illustrated by a closed white line. On the left and right sides of the inclusion, the temperature within the diffuse interface is elevated compared to the top and bottom sides, where elevated temperatures occur within the pure matrix, outside of the diffuse interface. An increase of the temperature leads to a reduction of the stress according to the thermoelastic Hooke's law, cf. Eq. (12). Thus, the stress and, thereby, the elastic energy, within the diffuse interface is reduced more to the left and right of the inclusion than above and below it. This leads to a higher speed of phase transition at the top and the bottom of the inclusion compared to the left and right side, causing the anisotropic growth behavior. Contrarily, the stress and, thus the elastic energy, is not affected by any thermal fields, cf. Eq. (24), regarding the TWT. Consequently, for TWT, the speed of phase transition is higher compared to TCT, cf. Fig. 3, and no anisotropic growth behavior induced, cf. Fig. 4.

Finally, the TCT yields an anisotropic growth of the inclusion due to the thermomechanical coupling, while the TWT yields an isotropic growth.

Thermomechanically coupled theory, influence on the shape of inclusion In this paragraph, the influence of the heat conduction on the shape of the inclusion is discussed. To this end, either the characteristic length scale of the problem, e.g., the initial diameter d_0, the characteristic time, or the value of the actual heat conductivity is changed,

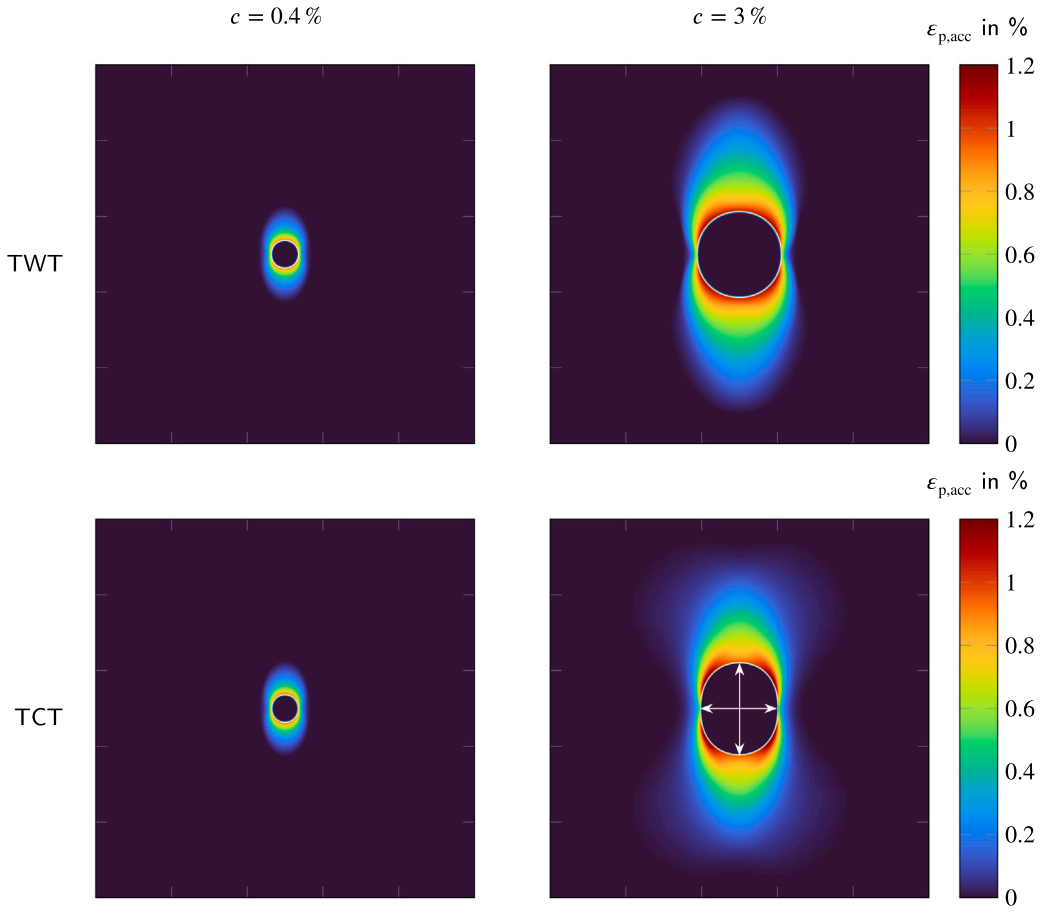

Fig. 4. Comparison of the accumulated plastic strain fields for the growing inclusion in the case of $\varepsilon^* = 1\%$. The simulation results for employing TWT (top) and TCT (bottom) are depicted at volume fraction $c = 0.4\%$ (left) and $c = 3\%$ (right). For TCT, the half axes of the elliptic anisotropy are indicated by white arrows. A phase-inherent plasticity without inheritance of plastic fields is considered. Thus, the accumulated plastic strain is vanishing within the inclusion and the inclusion stays completely elastic during the simulation. The closed white line illustrates the median of the diffuse interface.

cf. Appendix for details. Here, the latter approach is pursued and the conductivity $\alpha = 46\,\mathrm{kg\,m\,s^{-3}\,K^{-1}}$, used in the section above, is varied by multiplication with a factor $k \in \{0, 0.5, 1, 2, 4\}$. This study is conducted for an eigenstrain of $\varepsilon^* = 0.01$. Regarding a volume concentration of $c = 3\%$, the distribution of the temperature difference is illustrated in Fig. 6. Regarding $k = 0$, the heat conduction is completely neglected and, thus, the temperature difference, depicted at the bottom of Fig. 5, is a result of the accumulated source terms exclusively. The corresponding source term contributions are depicted in Fig. 7 of the Appendix. Throughout the whole process, the matrix is elastoplastic whereas the inclusion remains elastic, cf., e.g., [38,46]. Thus, for $k = 0$, the equation of heat conduction given by Eq. (19) reduces to

$$\rho\kappa_c\dot{\theta} = \gamma\,||\mathrm{dev}\,(\boldsymbol{\sigma})\,|| - 3K\alpha\theta\ \mathrm{tr}\,(\dot{\boldsymbol{\varepsilon}}), \quad \rho\kappa_c\dot{\theta} = -3K\alpha\theta\ \mathrm{tr}\,(\dot{\boldsymbol{\varepsilon}}), \tag{44}$$

for points outside and within the inclusion, respectively. Consequently, the temperature change within the inclusion is caused by the thermo-mechanical coupling contribution $p_{\mathrm{thm}} = -3K\alpha\theta\ \mathrm{tr}\,(\dot{\boldsymbol{\varepsilon}})$, a phenomenon referred to as Joule-Gough effect, cf., e.g., [75], [76, pp.456–461]. Outside of the inclusion, the change of temperature is caused by the interaction between the plastic stress power density $\gamma||\mathrm{dev}\,(\boldsymbol{\sigma})\,||$ and the contribution p_{thm}, where the plastic stress power density is a result of the displacive phase transformation of the austenitic matrix to martensite. Within the diffuse interface, all quantities are a mixture of the corresponding phase-inherent fields of both matrix and inclusion. Thus, plastic contributions are also present in the diffuse interface, while they become zero in regions of pure inclusion $\{\boldsymbol{x} \in \Omega : \phi_1(\boldsymbol{x}, t) = 1\}$. Regarding a non-vanishing coefficient of heat conduction, more heat transfer occurs, characterized by the decrease of temperature gradients, which is observed as expected. Consequently, with increasing thermal conductivity coefficient, the anisotropic growth decreases, cf. Table 4. The half axes ratio R_{yx} is smaller, the higher the heat conduction is. This can be associated with the smaller peak value of the temperature at the left and right flank of the inclusion and, thus, with a smaller decrease of the stress due to the thermoelastic Hooke's law according to Eq. (12).

Table 4
Based on the TCT simulations illustrated by Fig. 6, the values of the half axes ratio R_{yx} are compared for two volume concentrations $c = 0.4\,\%$ and $c = 3\,\%$ and different thermal conductivities $\kappa = k \cdot 46\,\mathrm{kg\,m\,s^{-3}\,K^{-1}}$ which are varied by a factor $k \in \{0, 0.5, 1, 2, 4\}$ at eigenstrain $\varepsilon^* = 1\,\%$. The depicted values of R_{yx} illustrate that the anisotropic growth decreases as the thermal conductivity coefficient increases.

k	R_{yx} for $c = 0.4\%$	R_{yx} for $c = 3\%$
0	1.0562	1.1666
0.5	1.0543	1.1588
1	1.0494	1.1414
2	1.0421	1.1405
4	1.0355	1.1396

Consequences with respect to the effective material properties Regarding a composite material, the effective properties are affected, among others, by the volume concentration and the shape of its constituents. This

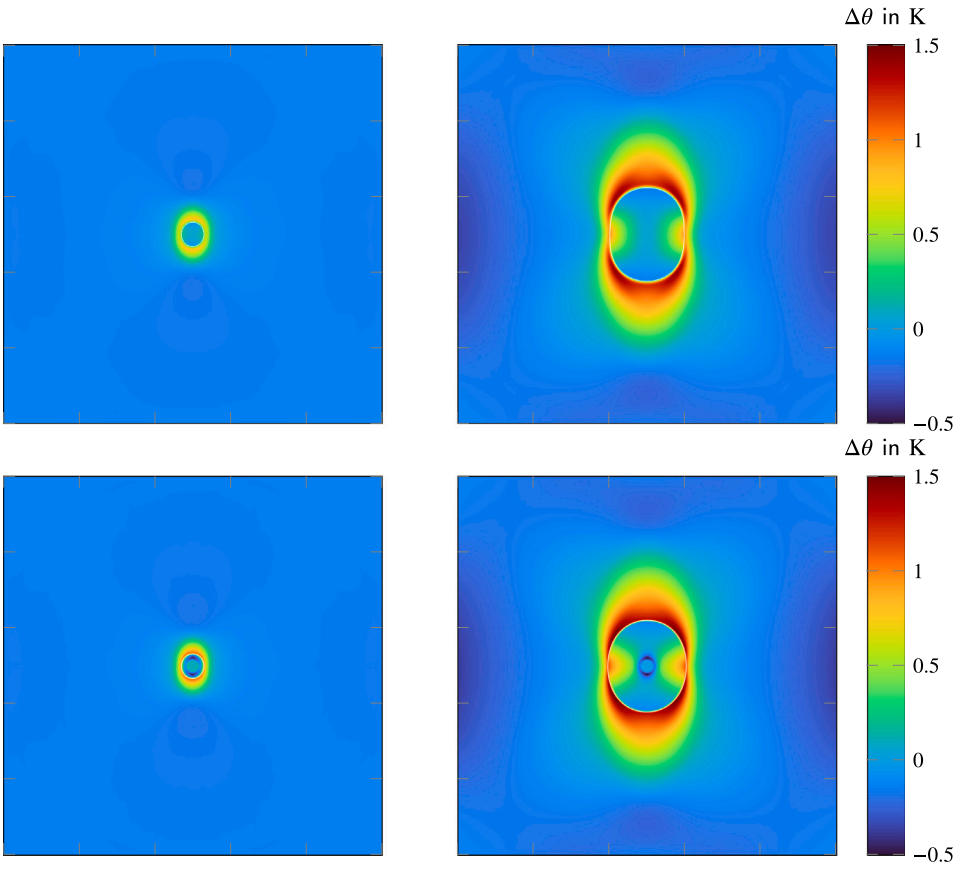

Fig. 5. Temperature distributions obtained by TCT simulations for $\varepsilon^* = 1\%$ at volume fraction $c = 0.4\%$ (left column) and $c = 3\%$ (right column). The influence of the coefficient of heat conduction on the temperature distribution is illustrated for different stages of the inclusion growth. For the top row, the coefficient of heat conduction is considered as stated in Table 2. In contrast, for the lower row a vanishing coefficient of heat conduction is considered, i.e., no heat conduction occurs.

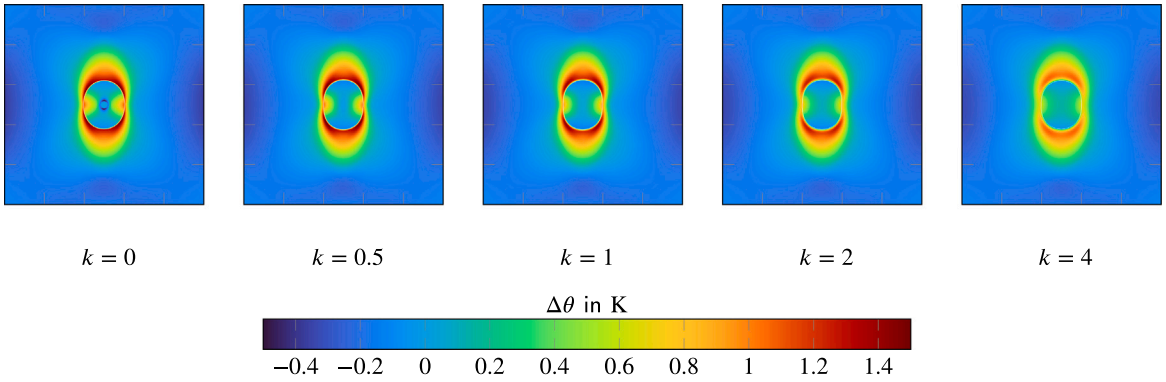

Fig. 6. Temperature distributions from TCT simulations compared for different thermal conductivities $\kappa = k \cdot 46\,\mathrm{kg\,m\,s^{-3}\,K^{-1}}$ varying by a factor $k \in \{0, 0.5, 1, 2, 4\}$ at eigenstrain $\varepsilon^* = 1\%$ and volume concentrations $c = 3\%$. The higher the coefficient of heat conduction, the more heat transfer occurs. Consequently, the temperature peaks within the complete diffuse interface region decrease. As a result, the effect of anisotropic growth decreases as the thermal conductivity coefficient increases.

becomes especially illustrative in regard of mean field homogenization schemes that account for Hill's polarization tensor, cf., e.g., [77], which accounts for the geometry of the inclusions, cf., e.g., [78]. Thus, the quantitative prediction of effective material properties based on a digital microstructure, obtained by simulations of microstructure evolution, is increased by considering the TCT instead of TWT.

4 Concluding remarks

Thermomechanically coupled vs weakly coupled theory The work at hand revisits the well known concept of a thermomechanically coupled theory (TCT) and a thermomechanically weakly coupled theory (TWT). Both approaches are used to simulate the growth of an elastoplastic inclusion using the multiphase-field method. The inclusion is subjected to an eigenstrain, within an elastoplastic matrix under load. This setup mimics a diffusionless, displacement-free phase transformation, such as martensitic transformation. The application of TCT results in a load-induced, anisotropic growth of the inclusion, which can be directly attributed to the temperature-induced stress fields due to the consideration of thermal strains in the thermoelastic Hooke's law in the context of TCT. This anisotropic inclusion growth cannot be reproduced by using the TWT: The TWT does not take into account thermal strains and, therefore, thermal stresses. In addition, it is shown that the smaller the coefficient of heat conduction the more pronounced the anisotropy

of the inclusion. Regarding the limiting case of a vanishing heat conduction, the heat sources and, thus, the change of the temperature within the inclusion and outside the inclusion can be attributed to different causes: Inside the inclusion it is governed by the Joule-Gough effect, while outside the inclusion, the interaction between the plastic stress power density and the thermomechanical coupling contribution causes the change.Obviously, for a non-vanishing heat conduction, this separation does not hold, because of the diffusive heat transport, since heat conduction is present. Furthermore, it is shown that the application of the TWT leads to a significant overestimation of the volume fraction of the inclusion compared to the TCT. Consequently, using a simplified example, the present work reveals that neglecting the thermomechanical coupling is not applicable when phase transformations are considered and the coefficient of thermal expansion is not negligible.

Consequences regarding the prediction of effective material parameters The main objectives of the simulations are the prediction of the volume concentration of the inclusion for a specific simulation time as well as of the shape of the inclusion due to microstructure evolution and, thereby, of the obtained morphology. Both the volume concentration of inclusions and their shape significantly affect the effective material behavior. Since the TWT overestimates the volume concentration compared to the TCT and the TCT accounts for the anisotropic growth of the inclusion, using the TCT yields more quantitative results than the TWT.

CRediT authorship contribution statement

Andreas Prahs: Conzeptualization, Formal analysis, Investigation, Methodology, Validation, Writing – original draft, Writing – review & editing. **Martin Reder:** Formal analysis, Investigation, Software, Validation, Writing – original draft, Writing – review & editing, Visualization. **Daniel Schneider:** Conzeptualization, Investigation, Writing – review & editing, Supervision. **Britta Nestler:** Writing – review & editing, Supervision, Funding acquisition.

Declaration of competing interest

The authors declare that they have no known competing financial interests or personal relationships that could have appeared to influence the work reported in this paper.

Data availability

Data will be made available on request.

Acknowledgments

The financial support of KIT excellence strategy ExU-Future Fields Stage 3 “Kadi4Mat” is gratefully acknowledged. In addition, support from KIT excellence strategy ExU-Future Fields Stage 2 “ACDC”, enabling meetings for intensive intellectual exchange on continuum thermodynamics, is also gratefully acknowledged. Contributions related to the model formulations and evaluations are provided through the “Materials Science and Engineering (MSE)” program No. 43.31.01, supported by the Helmholtz association, which is gratefully acknowledged. Implementation of the models were realized with partial financial support by the Bundesministerium für Bildung und Forschung (BMBF) within the KMU-innovative project BioSorb.

Appendix

Heat conduction in the context of TCT Inserting the material time derivative of the Legendre transformation, i.e., $\dot{e} = \dot{\psi} + \dot{\theta}\eta + \theta\dot{\eta}$, in the balance of internal energy according to Eq. (4) yields

$$\rho\dot{\psi} + \rho\dot{\theta}\eta + \rho\theta\dot{\eta} = \rho r + \boldsymbol{\sigma}\cdot\dot{\boldsymbol{\varepsilon}} - \operatorname{div}(\boldsymbol{q})\,. \tag{45}$$

Accounting for Eq. (8), Eq. (45) reads

$$\left(\rho\frac{\partial\psi}{\partial\boldsymbol{\varepsilon}} - \boldsymbol{\sigma}\right)\cdot\dot{\boldsymbol{\varepsilon}} + \rho\frac{\partial\psi}{\partial\boldsymbol{\varepsilon}^{\mathrm{p}}}\cdot\dot{\boldsymbol{\varepsilon}}^{\mathrm{p}} + \rho\left(\eta + \frac{\partial\psi}{\partial\theta}\right)\cdot\dot{\theta} + \rho\theta\dot{\eta} = \rho r - \operatorname{div}(\boldsymbol{q})\,. \tag{46}$$

Taking into account the potential relations for the Cauchy stress tensor $\boldsymbol{\sigma}$ as well as for the entropy η according to Eq. (10), as well as Eq. $(12)_2$, Eq. (46) yields

$$-\boldsymbol{\sigma}\cdot\dot{\boldsymbol{\varepsilon}}^{\mathrm{p}} + \rho\theta\dot{\eta} = \rho r - \operatorname{div}(\boldsymbol{q})\,. \tag{47}$$

Due to the potential relation for the entropy given by Eq. $(10)_2$, the material time derivative of the entropy is given by

$$\dot{\eta} = \left(-\frac{\partial\psi}{\partial\theta}\right)^{\cdot} = -\frac{\partial\dot{\psi}}{\partial\theta} = -\frac{\partial^2\psi}{\partial\boldsymbol{\varepsilon}\partial\theta}\cdot\dot{\boldsymbol{\varepsilon}} - \frac{\partial^2\psi}{\partial\boldsymbol{\varepsilon}^{\mathrm{p}}\partial\theta}\cdot\dot{\boldsymbol{\varepsilon}}^{\mathrm{p}} - \frac{\partial^2\psi}{\partial\theta^2}\dot{\theta}. \tag{48}$$

Accounting for Eq. (48), Eq. (47) can be written as

$$-\boldsymbol{\sigma}\cdot\dot{\boldsymbol{\varepsilon}}^{\mathrm{p}} - \rho\theta\left(\frac{\partial^2\psi}{\partial\boldsymbol{\varepsilon}\partial\theta}\cdot\dot{\boldsymbol{\varepsilon}} + \frac{\partial^2\psi}{\partial\boldsymbol{\varepsilon}^{\mathrm{p}}\partial\theta}\cdot\dot{\boldsymbol{\varepsilon}}^{\mathrm{p}} + \frac{\partial^2\psi}{\partial\theta^2}\dot{\theta}\right) = \rho r - \operatorname{div}(\boldsymbol{q})\,. \tag{49}$$

Considering again the potential relations according to Eq. (10), Eq. (49) reads

$$-\boldsymbol{\sigma}\cdot\dot{\boldsymbol{\varepsilon}}^{\mathrm{p}} - \theta\frac{\partial\boldsymbol{\sigma}}{\partial\theta}\cdot\dot{\boldsymbol{\varepsilon}} + \theta\frac{\partial\boldsymbol{\sigma}}{\partial\theta}\cdot\dot{\boldsymbol{\varepsilon}}^{\mathrm{p}} - \rho\theta\frac{\partial^2\psi}{\partial\theta^2}\dot{\theta} = \rho r - \operatorname{div}(\boldsymbol{q})\,. \tag{50}$$

Non-dimensionalized form of governing equations Let $(\cdot)^*$ and $(\cdot)_{\mathrm{c}}$ denote dimensionless and characteristic quantities, respectively. Each quantity arising in the governing equation can be split into a product of its dimensionless quantity and a characteristic value. This yields

$$0 = \operatorname{div}^*\left(\boldsymbol{\sigma}^*\right) \tag{51}$$

$$\frac{\rho\kappa_{\mathrm{c}}\theta_{\mathrm{c}}}{t_{\mathrm{c}}}\frac{\partial\theta^*}{\partial t^*} = \frac{\kappa\theta_{\mathrm{c}}}{l_{\mathrm{c}}^2}\triangle^*\left(\theta^*\right) + \frac{\sigma_{\mathrm{c}}}{t_{\mathrm{c}}}\boldsymbol{\sigma}^*\cdot\dot{\boldsymbol{\varepsilon}}^{\mathrm{p}*} - \frac{\alpha\theta_{\mathrm{c}}\sigma_{\mathrm{c}}}{t_{\mathrm{c}}}\theta^*\left(\mathbb{C}^*\left[\boldsymbol{I}\right]\right)\cdot\left(\dot{\boldsymbol{\varepsilon}}^* - \dot{\boldsymbol{\varepsilon}}^{\mathrm{p}*}\right) \tag{52}$$

$$\frac{\partial\phi}{\partial t^*} = -\frac{t_{\mathrm{c}}M\gamma}{l_{\mathrm{c}}^2}\left[\frac{16}{(\pi\epsilon^*)^2}(1-2\phi) - 2\triangle^*\left(\phi\right)\right] + \frac{t_{\mathrm{c}}M\sigma_{\mathrm{c}}}{l_{\mathrm{c}}}\frac{1}{\epsilon^*}\left(\rho_2\psi_2 - \rho_1\psi_1\right)^*. \tag{53}$$

From the heat conduction equation (52) it can be seen, that the characteristic length scale l_{c} only arises in the heat conduction term. Additionally, the inverse of the characteristic time t_{c} occurs in all terms except the heat conduction term. Therefore, the influence of heat conductivity is increased relative to the other contributions, if the length scale gets smaller, or alternatively a larger time scale, and, thus, a slower process velocity is considered. The interface velocity and, thus, the speed of the phase transformation can be controlled by the mobility parameter M, if both characteristic time and stress are given. The consideration of the stationary momentum balance (51) instead of the dynamic one $\frac{\rho l_{\mathrm{c}}}{t_{\mathrm{c}}^2}\frac{\partial^2\boldsymbol{u}^*}{\partial t^{*2}} = \frac{\sigma_{\mathrm{c}}}{l_{\mathrm{c}}}\operatorname{div}^*(\boldsymbol{\sigma}^*)$ is justified, if $\mathcal{O}\left(l_{\mathrm{c}}^2/(\sigma_{\mathrm{c}}t_{\mathrm{c}}^2)\right) \ll 1$ holds. This is the case in the present work, since the considered set of parameters yields an order of magnitude 1×10^{-4}.

Heat source contributions The total heat source generally consists of both the thermomechanical coupling contribution and the plastic stress power. However, only for vanishing heat conduction it is possible to additively decompose the temperature distribution into the accumulation of these two contributions, since no heat transfer occurs. This is done in the following. From Fig. 7, the following observations can be made:

- Within the inclusion, all strains are almost constant in time.

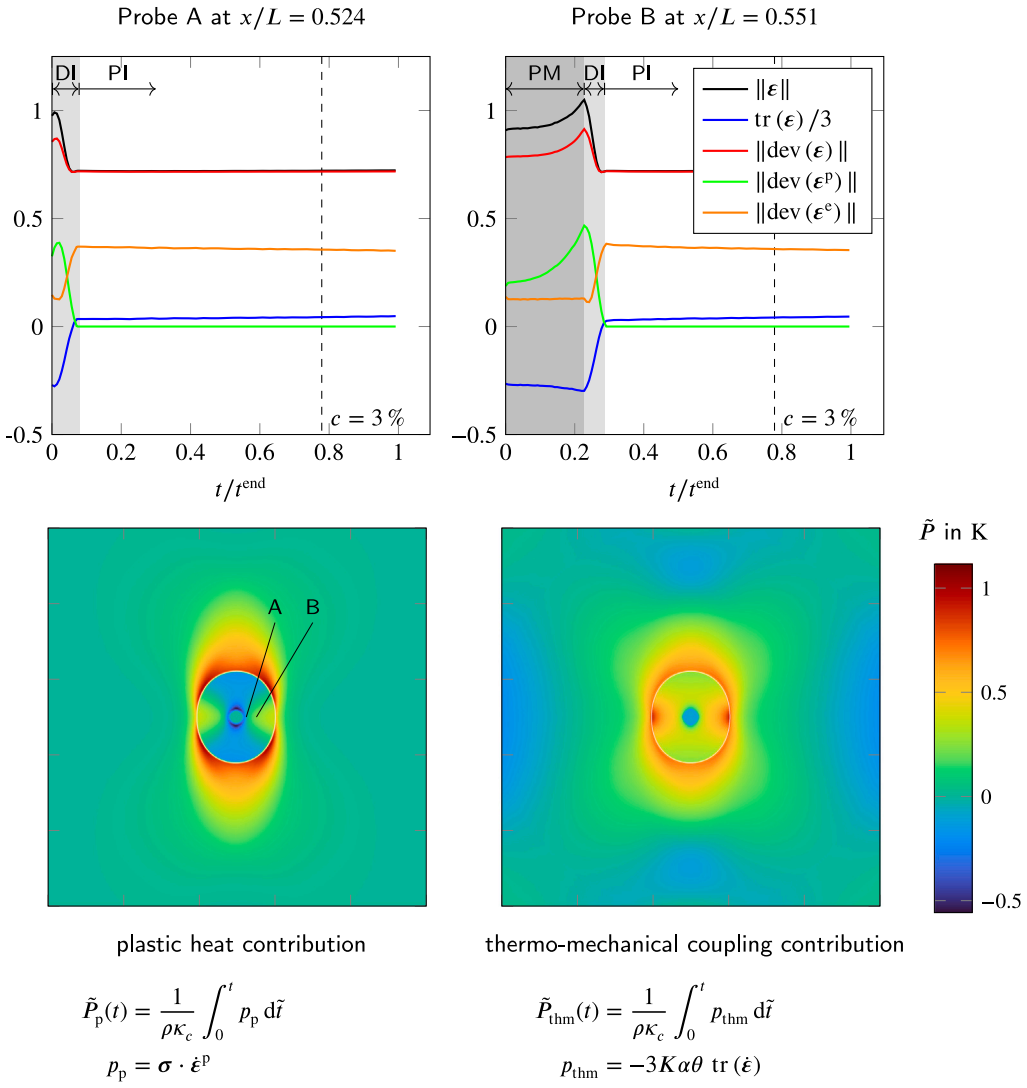

Fig. 7. Details of TCT simulation excluding heat conduction at eigenstrain $\varepsilon^* = 1\%$. Top: Temporal evolution of strain quantities at two probe locations A and B. The phase, the probe position belongs to is indicated by PM for pure matrix ($\phi_{\mathrm{m}} = 1$), DI for diffuse interface region ($\phi_{\mathrm{m}} \in (0, 1)$) and PI for pure inclusion ($\phi_{\mathrm{m}} = 0$). Bottom: Field information for the contribution of plastic heat supply and thermomechanical coupling by means of time integrated source terms p_{p} and p_{thm} normalized by $\rho\kappa_c$. The snapshots are given at $c = 3\%$ and the probe location is plotted in the left one.

- The total strain in the inclusion is mainly deviatoric.
- The coupling contribution yields a heating inside the inclusion at the locations of maximum compression stress, which are the left and right sides of the inclusion. At the same locations the temperature is also increased within the diffuse interface. The elevated temperature decreases the stress at these particular locations compared to a TWT. This is a reason for the anisotropic growth behavior.
- Within the matrix, the plastic strain raises in time inducing a (positive) plastic power.
- As soon as a point undergoes phase transformation, the total plastic strain decreases. This is due to a decreasing matrix phase ($\dot{\phi}_{\mathrm{m}} < 0$), which exhibits non-zero phase-inherent plastic strain. At the same time, the inclusion phase increases, but its phase-inherent plastic strain is zero. This effect induces a negative plastic power.
- Whether the overall plastic work in a point is positive or negative, depends on which of the effects is dominant. For instance, for sample A, the phase transformation happens early on, since the point is near the inclusion. Thus, the second effect dominates leading to an effective cooling. For sample B initially more far away from the inclusion, the first effect dominates leading to an effective heating.

References

[1] Lemaitre J, Chaboche JL. Mechanics of solid materials. Repr. ed.. Cambridge: Cambridge Univ. Press; 2000.

[2] Zubelewicz A. Century-long Taylor-Quinney interpretation of plasticity-induced heating reexamined. Sci Rep 2019;9:1–7.

[3] Morin C, Moumni Z, Zaki W. A constitutive model for shape memory alloys accounting for thermomechanical coupling. Int J Plast 2011a;27:748–67.

[4] Morin C, Moumni Z, Zaki W. Thermomechanical coupling in shape memory alloys under cyclic loadings: Experimental analysis and constitutive modeling. Int J Plast 2011b;27:1959–80.

[5] Mahnken R, Wolff M, Schneidt A, Böhm M. Multi-phase transformations at large strains – thermodynamic framework and simulation. Int J Plast 2012;39:1–26.

[6] Klusemann B, Fischer G, Böhlke B. Thermomechanical characterization of portevin–le châtelier bands in AlMg3 (AA5754) and modeling based on a modified Estrin–McCormick approach. Int J Plast 2015;67:192–216.

[7] Wang J, Moumni Z, Zhang W. A thermomechanically coupled finite-strain constitutive model for cyclic pseudoelasticity of polycrystalline shape memory alloys. Int J Plast 2017;97:194–221.

[8] Tang T, Zhou G, Li Z, Li D, Peng L, Peng Y, Wu P, Wang H, Lee MG. A polycrystal plasticity based thermo-mechanical-dynamic recrystallization coupled modeling method and its application to light weight alloys. Int J Plast 2019;116:159–91.

[9] Li J, Romero I, Segurado J. Development of a thermo-mechanically coupled crystal plasticity modeling framework: Application to polycrystalline homogenization. Int J Plast 2019;119:313–30.

[10] Wulfinghoff S, Bayerschen E, Böhlke T. A gradient plasticity grain boundary yield theory. Int J Plast 2013;51:33–46.

[11] Bayerschen E, Prahs A, Wulfinghoff S, Ziemann M, Gruber PA, Walter M, Böhlke T. Modeling contrary size effects of tensile- and torsion-loaded oligocrystalline gold microwires. J Mater Sci 2016;51:7451–70.

[12] Steinbach I, Pezzolla F, Nestler B, Seeßelberg M, Prieler R, Schmitz G, Rezende J. A phase field concept for multiphase systems. Physica D 1996;94:135–47.

[13] Steinbach I, Pezzolla F. A generalized field method for multiphase transformations using interface fields. Physica D 1999;134:385–93.

[14] Nestler B, Garcke H, Stinner B. Multicomponent alloy solidification: phase-field modeling and simulations. Phys Rev E 2005;71:041609.

[15] Nestler B, Choudhury A. Phase-field modeling of multi-component systems. Curr Opin Solid State Mater Sci 2011;15:93–105.

[16] Steinbach I. Phase-field model for microstructure evolution at the mesoscopic scale. Annu Rev Mater Res 2013;43:89–107.

[17] Ambati M, Gerasimov T, De Lorenzis L. A review on phase-field models of brittle fracture and a new fast hybrid formulation. Comput Mech 2015;55:383–405.

[18] Beckermann C, Diepers HJ, Steinbach I, Karma A, Tong X. Modeling melt convection in phase-field simulations of solidification. J Comput Phys 1999;154:468–96.

[19] Wheeler AA, Boettinger WJ, McFadden GB. Phase-field model for isothermal phase transitions in binary alloys. Phys Rev A 1992;45(7424).

[20] Chen Q, Ma N, Wu K, Wang Y. Quantitative phase field modeling of diffusion-controlled precipitate growth and dissolution in ti–al–v. Scr Mater 2004;50:471–6.

[21] Kim K, Roy A, Gururajan M, Wolverton C, Voorhees P. First-principles/phase-field modeling of θ' precipitation in al-cu alloys. Acta Mater 2017;140:344–54.

[22] Moelans N, Godfrey A, Zhang Y, Jensen DJ. Phase-field simulation study of the migration of recrystallization boundaries. Phys Rev B 2013;88:054103.

[23] Takaki T, Yoshimoto C, Yamanaka A, Tomita Y. Multiscale modeling of hot-working with dynamic recrystallization by coupling microstructure evolution and macroscopic mechanical behavior. Int J Plast 2014;52:105–16.

[24] Zhao P, Song En Low T, Wang Y, Niezgoda SR. An integrated full-field model of concurrent plastic deformation and microstructure evolution: Application to 3d simulation of dynamic recrystallization in polycrystalline copper. Int J Plast 2016;80:38–55.

[25] Schöller L. Schneider D, Herrmann C, Prahs A, Nestler B. Phase-field modeling of crack propagation in heterogeneous materials with multiple crack order parameters. Comput Methods Appl Mech Engrg 2022;395:114965.

[26] Schöller L. Schneider D, Prahs A, Nestler B. Phase-field modeling of crack propagation based on multi-crack order parameters considering mechanical jump conditions. PAMM 2023;22:e202200039.

[27] Ruan H, Rezaei S, Yang Y, Gross D, Xu BX. A thermo-mechanical phase-field fracture model: Application to hot cracking simulations in additive manufacturing. J Mech Phys Solids 2023;172:105169.

[28] Penrose O, Fife PC. Thermodynamically consistent models of phase-field type for the kinetic of phase transitions. Physica D 1990;43:44–62.

[29] Fried E, Gurtin ME. Continuum theory of thermally induced phase transitions based on an order parameter. Physica D 1993;68:326–43.

[30] Gurtin ME. Generalized ginzburg-landau and cahn-hilliard equations based on a microforce balance. Physica D 1996;92:178–92.

[31] Wang S, Zaeem MA, Horstemeyer MF, Wang PT. Investigating thermal effects on morphological evolution during crystallisation of hcp metals: three-dimensional phase field study. Mater Technol 2012;27:355–63.

[32] Cissé C, Asle Zaeem M. An asymmetric elasto-plastic phase-field model for shape memory effect, pseudoelasticity and thermomechanical training in polycrystalline shape memory alloys. Acta Mater 2020;201:580–95.

[33] Cui S, Wan J, Zuo X, Chen N, Zhang J, Rong Y. Three-dimensional, non-isothermal phase-field modeling of thermally and stress-induced martensitic transformations in shape memory alloys. Int J Solids Struct 2017;109:1–11.

[34] Greenwood GW, Johnson R. The deformation of metals under small stresses during phase transformations. Proc R Soc Lond Ser A 1965;283:403–22.

[35] Fischlschweiger M, Cailletaud G, Antretter T. A mean-field model for transformation induced plasticity including backstress effects for non-proportional loadings. Int J Plast 2012;37:53–71.

[36] Raabe D, Ponge D, Dmitrieva O, Sander B. Designing ultrahigh strength steels with good ductility by combining transformation induced plasticity and martensite aging. Adv Energy Mater 2009;11:547–55.

[37] Li Z, Pradeep KG, Deng Y, Raabe D, Tasan CC. Metastable high-entropy dual-phase alloys overcome the strength–ductility trade-off. Nature 2016;534:227–30.

[38] Leblond J, Devaux J, Devaux J. Mathematical modelling of transformation plasticity in steels i: Case of ideal-plastic phases. Int J Plast 1989;5:551–72.

[39] Khan AS, Liu J, Yoon JW, Nambori R. Strain rate effect of high purity aluminum single crystals: Experiments and simulations. Int J Plast 2015;67:39–52.

[40] Khan AS, Liu J. A deformation mechanism based crystal plasticity model of ultrafine-grained/nanocrystalline fcc polycrystals. Int J Plast 2016;86:56–69.

[41] Cyr ED, Mohammadi M, Mishra RK, Inal K. A three dimensional (3d) thermo-elasto-viscoplastic constitutive model for fcc polycrystals. Int J Plast 2015;70:166–90.

[42] Cyr E, Mohammadi M, Brahme A, Mishra RK, Inal K. Modeling the formability of aluminum alloys at elevated temperatures using a new thermo-elasto-viscoplastic crystal plasticity framework. Int J Mech Sci 2017;128–129:312–25.

[43] Yu C, Kang G, Kan Q, Song D. A micromechanical constitutive model based on crystal plasticity for thermo-mechanical cyclic deformation of niti shape memory alloys. Int J Plast 2013;44:161–91.

[44] Petersmann M, Antretter T, Cailletaud G, Sannikov A, Ehlenbröker F. Unification of the non-linear geometric transformation theory of martensite and crystal plasticity - application to dislocated lath martensite in steels. Int J Plast 2019;119:140–55.

[45] Connolly D, Kohar C, Inal K. A novel crystal plasticity model incorporating transformation induced plasticity for a wide range of strain rates and temperatures. Int J Plast 2022;152:103188.

[46] Leblond J, Mottet G, Devaux J. A theoretical and numerical approach to the plastic behaviour of steels during phase transformations—i. derivation of general relations. J Mech Phys Solids 1986;34:395–409.

[47] Levitas VI. Phase-field theory for martensitic phase transformations at large strains. Int J Plast 2013;49:85–118.

[48] Levitas VI. Phase field approach to martensitic phase transformations with large strains and interface stresses. J Mech Phys Solids 2014;70:154–89.

[49] Levitas VI. Phase field approach for stress- and temperature-induced phase transformations that satisfies lattice instability conditions. part i. general theory. Int J Plast 2018;106:164–85.

[50] Mamivand M, Zaeem MA, El Kadiri H. A review on phase field modeling of martensitic phase transformation. Comput Mater Sci 2013;77:304–11.

[51] Mahnken R, Schneidt A, Antretter T, Ehlenbröker M. Multi-scale modeling of bainitic phase transformation in multi-variant polycrystalline low alloy steels. Int J Solids Struct 2015;54:156–71.

[52] Cheng C, Mahnken R. Extension of a multi-mechanism model: Hardness-based flow and transformation induced plasticity for austenitization. Int J Solids Struct 2016;102–103:127–41.

[53] Kubler R, Berveiller M, Buessler P. Semi phenomenological modelling of the behavior of trip steels. Int J Plast 2011;27:299–327.

[54] Lai Q, Brassart L, Bouaziz O, Gouné M, Parry G, Perlade A, Bréchet T. Influence of martensite volume fraction and hardness on the plastic behavior of dual-phase steels: Experiments and micromechanical modeling. Int J Plast 2016;80:187–203.

[55] Ismail K, Perlade A, Jacques PJ, Pardoen T, Brassart L. Impact of second phase morphology and orientation on the plastic behavior of dual-phase steels. Int J Plast 2019;118:130–46.

[56] Pierman AP, Bouaziz O, Pardoen T, Jacques P, Brassart L. The influence of microstructure and composition on the plastic behaviour of dual-phase steels. Acta Mater 2014;73:298–311.

[57] Marsden JE, Hughes TJR. Mathematical foundations of elasticity. New York: Dover; 1994.

[58] Prahs A, Böhlke T. On invariance properties of an extended energy balance. Contin Mech Thermodyn 2019b;32:843–59.

[59] Prahs A, Böhlke T. On interface conditions on a material singular surface. Contin Mech Thermodyn 2019a;32:1417–34.

[60] Maugin GA. The thermomechanics of plasticity and fracture. Cambride: Cambridge University Press; 1992.

[61] Coleman BD, Gurtin ME. Thermodynamics with internal state variables. J Chem Phys 1967;47:597–613.

[62] Beegle BL, Modell M, Reid RC. Legendre transforms and their application in thermodynamics. AIChE J 1974;20:1194–200.

[63] Neumann R, Böhlke T. Hashin–Shtrikman type mean field model for the two-scale simulation of the thermomechanical processing of steel. Int J Plast 2016;77:1–29.

[64] Prahs A, Böhlke T. The role of dissipation regarding the concept of purely mechanical theories in plasticity. Mech Res Commun 2021;119:103832.

[65] Simo J, Hughes T. Computational inelasticity. New York: Springer; 2008.

[66] Bertram A. Elasticity and plasticity of large deformations: an introduction. Berlin: Springer; 2005.

[67] Moelans N, Blanpain B, Wollants P. An introduction to phase-field modeling of microstructure evolution. Calphad - Comput Coupling Phase Diagr Thermochem 2008;32:268–94.

[68] Herrmann C, Schoof E, Schneider D, Schwab F, Reiter A, Selzer M, Nestler B. Multiphase-field model of small strain elasto-plasticity according to the mechanical jump conditions. Comput Mech 2018;62:1399–412.

[69] Hoffrogge P, Mukherjee A, Nani E, Amos PK, Wang F, Schneider D, Nestler B. Multiphase-field model for surface diffusion and attachment kinetics in the grand-potential framework. Phys Rev E 2021;103:033307.

[70] Khachaturyan AG. Theory of structural transformations in solids. New York, NY: John Wiley and Sons; 1983.

[71] Schneider D, Schoof E, Tschukin O, Reiter A, Herrmann C, Schwab F, Selzer M, Nestler B. Small strain multiphase-field model accounting for configurational forces and mechanical jump conditions. Comput Mech 2018;61:277–95.

[72] Goldstein H, Poole CP, Safko JL. Classical mechanics. 3rd ed.. San Francisco: Addison Wesley; 2002.

[73] Schoof E, Herrmann C, Streichhan N, Selzer M, Schneider D, Nestler B. On the multiphase-field modeling of martensitic phase transformation in dual-phase steel using J_2-viscoplasticity. Modelling Simul Mater Sci Eng 2019;27:025010.
[74] Hötzer J. Reiter A, Hierl H, Steinmetz P, Selzer M, Nestler B. The parallel multi-physics phase-field framework PACE3D. J Comput Sci 2018;26:1–12.
[75] Schweizer B, Wauer J. Atomistic explanation of the Gough-Joule-effect. Eur Phys J B 2001;23:383–90.
[76] Willner K. Kontinuums- und Kontaktmechanik: Synthetische und analytische Darstellung. New York: Springer; 2003.
[77] Willis J. Variational and related methods for the overall properties of composites. In: Yih CS, editor. Advances in applied mechanics. Advances in applied mechanics, Vol. 21, Elsevier; 1981, p. 1–78.
[78] Kehrer L, Wood JT, Böhlke T. Mean-field homogenization of thermoelastic material properties of a long fiber-reinforced thermoset and experimental investigation. J Compos Mater 2020;54:3777–99.